Matter

CellPress

Article

Understanding the ligand-assisted reprecipitation of $CsPbBr_3$ nanocrystals via high-throughput robotic synthesis approach

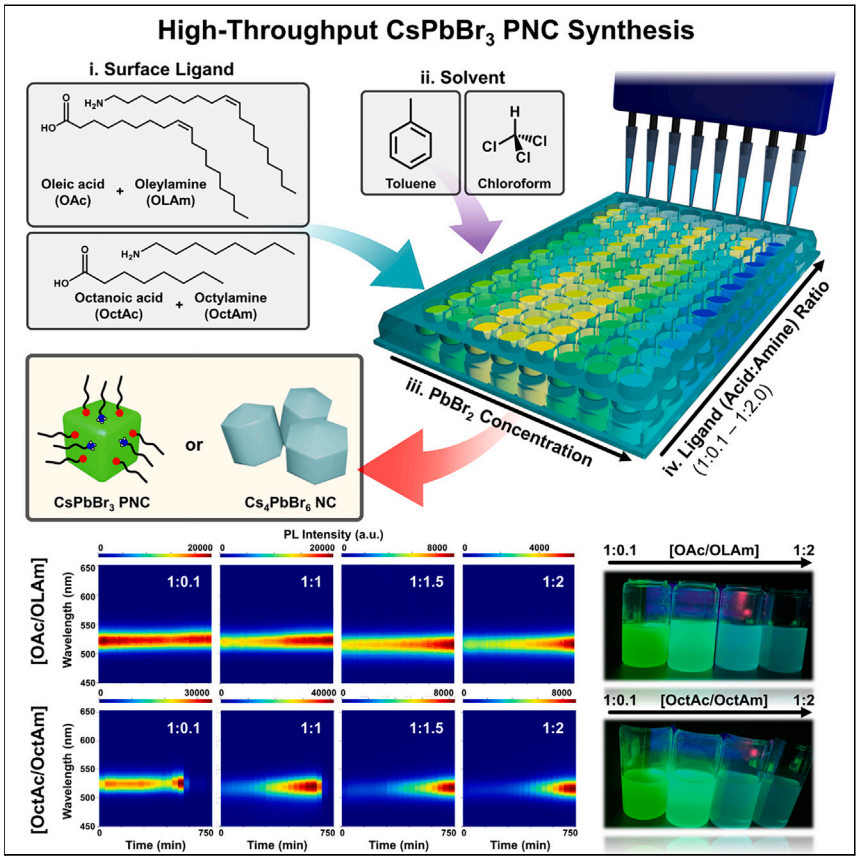

This study explores the use of ligand-assisted reprecipitation (LARP) as an alternative method for mass production of perovskite nanocrystals (PNCs), in combination with high-throughput synthesis, automated characterization, and machine learning. The study systematically explores the influence of chemical and processing parameters on the growths, structures, and functionalities of the PNCs. A mechanism in which ligand diffusion during crystallization determines the PNC structures and functionalities is proposed. This approach paves the way to explore in-depth chemistry and processing optimization of PNC synthesis.

Improvement
Enhanced performance with innovative design or material control

Sheryl L. Sanchez, Yipeng Tang, Bin Hu, Jonghee Yang, Mahshid Ahmadi

jyang70@utk.edu (J.Y.)
mahmadi3@utk.edu (M.A.)

Highlights

High-throughput automated experimental workflow for LARP-PNC synthesis is employed

Effects of chemical and processing parameters on PNC functionalities are explored

SHAP, a machine learning method, assesses the impact of synthesis parameters

Ligand diffusion during reaction determines the functionalities of PNCs

Sanchez et al., Matter 6, 1–19
September 6, 2023
https://doi.org/10.1016/j.matt.2023.05.023

Please cite this article in press as: Sanchez et al., Understanding the ligand-assisted reprecipitation of $CsPbBr_3$ nanocrystals via high-throughput robotic synthesis approach, Matter (2023), https://doi.org/10.1016/j.matt.2023.05.023

Matter

CellPress

Article

Understanding the ligand-assisted reprecipitation of $CsPbBr_3$ nanocrystals via high-throughput robotic synthesis approach

Sheryl L. Sanchez,[1] Yipeng Tang,[1] Bin Hu,[1] Jonghee Yang,[1,*] and Mahshid Ahmadi[1,2,*]

SUMMARY

Inorganic cesium lead bromide ($CsPbBr_3$) perovskite nanocrystals (PNCs) have shown promise in optoelectronic applications. A simpler method of synthesizing high-quality PNCs is the ligand-assisted reprecipitation (LARP) method, but it is susceptible to instability. This study used a high-throughput automated experimental platform to explore the growth behaviors and colloidal stability of LARP-synthesized PNCs. The influence of ligands on particle growth and functionalities was systematically explored using two distinctive acid-base pairs. The study found that short-chain ligands cannot make functional PNCs with the desired sizes and shapes, whereas long-chain ligands provide homogeneous and stable PNCs. The study also found that excessive amines or polar antisolvents can cause PNCs to transform into a Cs-rich non-perovskite structure with poorer emission functionalities and larger size distributions. The diffusion of ligands in a reaction system is crucial in determining the structures and functionalities of the PNCs. This study provides detailed guidance on synthesis routes for desired PNCs.

INTRODUCTION

Lead halide perovskite nanocrystals (PNCs) are one of the most promising materials for use in optoelectronic applications including photovoltaics and light-emitting diodes.[1–5] This is due to their excellent optical characteristics being tunable across a wide band-gap range and their solution processability. All-inorganic cesium lead bromide ($CsPbBr_3$) NCs demonstrate narrow emission bands, high photoluminescence quantum yields, and great intrinsic stability[6–9] compared with their organic metal halide perovskite counterparts, which lack long-term stability under ambient conditions.

Conventionally, PNCs have been synthesized via hot-injection method by adding the precursor stock in a reaction flask in an elevated temperature and inert atmosphere. The resulting PNCs reproducibly exhibit narrow size distributions and excellent optical characteristics that are directed to device applications. However, the hot-injection method requires a dedicated reaction system and a sequence of multiple steps in a synthetic procedure that are complex, energy inefficient, and, essentially, not suited for mass production.

In contrast, the ligand-assisted reprecipitation (LARP) method is proposed as a promising alternative in the mass-producible PNC synthesis route, which simply synthesizes the PNCs having compatible functionalities.[10–12] Particularly, the simple synthetic procedure without requiring a complex infrastructure enables low-cost

PROGRESS AND POTENTIAL

The ligand-assisted reprecipitation (LARP) method for the synthesis of perovskite nanocrystals (PNCs) has recently garnered significant attention due to its feasibility in mass production. However, LARP synthesis is susceptible, and thus little has been deeply understood about how to control the growth of PNCs and the optical characteristics of the PNCs. In this study, by implementing a high-throughput automated experimental work, we explore the growth behaviors and colloidal stability of the LARP-synthesized PNCs. We systematically explore the influence of chemical and processing parameters on the growths and functionalities of the PNCs. In addition, the machine learning method assesses the impact of each synthesis parameter on PNC functionalities. Overall, we propose that the diffusion of the ligands in a reaction system crucially determines the structures and functionalities of the PNCs. Our high-throughput exploration provides detailed guidance on synthesis routes for desired PNCs.

Please cite this article in press as: Sanchez et al., Understanding the ligand-assisted reprecipitation of $CsPbBr_3$ nanocrystals via high-throughput robotic synthesis approach, Matter (2023), https://doi.org/10.1016/j.matt.2023.05.023

upscaling to commercial batches. However, the resulting PNCs are relatively susceptible in several post-processes, somewhat losing the desired functionalities for high-performance device applications. Thus, little has been understood about how the ligand properties, ratio, and solvent properties determine the overall size, shape, and stability of PNCs synthesized by the LARP method.

Herein, high-throughput screening allows for the variability of the synthesis routes to be explored within a few hours, rather than weeks and months, of optimization. The underlying mechanism behind the size, shape, and stability control of the NCs is explored through time-dependent photoluminescence (PL) and absorption spectroscopies. Using two unique acid-base ligand pairs—oleic acid-oleylamine and octanoic acid-octylamine—we systematically studied the influence of ligands—chain lengths, concentrations, and ratios—on particle growth and subsequent functionalities of PNCs. The desired size and shape of the PNCs were successfully produced by the long-chain ligands, providing uniform and stable NCs. The use of excessive amines or polar antisolvents was found to transform the PNCs into Cs-rich non-perovskite structures that exhibit larger size distributions and lower emission functions. These features are an indication that the ionic diffusion of ligands in a reaction system determines the structures and functions of the PNCs. Crucially, these results are also counterevidence against the common notion that the use of polar solvents for dissolving inorganic precursors (e.g., *N*,*N*-dimethylformamide [DMF]) is detrimental to PNC stability; rather, selection of antisolvent can be more critical. Our high-throughput exploration provides accelerated detailed instructions on the synthesis paths for the desired PNCs.

RESULTS AND DISCUSSION

Understanding and controlling the surface chemistry and properties of $CsPbBr_3$ PNCs are critical challenges, since the surface properties of PNCs can significantly affect their stability, reactivity, and optical properties. Recent studies have focused on understanding the unique chemical activities of different ligand types and additives that can modify their sizes/shapes and provide defect passivation.[13–16] These modifications can result in different surface energy levels and changes in band gap and can provide colloidal stability.[17–22] Each ligand type is utilized due to its unique chemical action—depending on its molecular structure and reactivity,[17,18,20,23] which not only influence the reaction pathway during synthesis but also the colloidal stability of the resulting PNCs.[24] Carboxylic acids and amines are commonly used in the synthesis of NCs to prevent aggregation and control crystallization, respectively.[25–27] Note that both carboxylic acids and amines are complementary to each other for PNC synthesis; mixing carboxylic acid and amine results in an intermolecular proton transfer from the acid to amine, transforming them to ionic carboxylate and ammonium, which can coordinate to the PNC surface.

High-throughput exploration on the growth behaviors of LARP-synthesized $CsPbBr_3$ PNCs was performed by utilizing an integrated automated synthesis-characterization system.[28] The high-throughput LARP synthesis was performed using the OT-II pipetting robot (Opentron) by injecting the $PbBr_2$ solutions (in DMF) with various $PbBr_2$ concentrations and the ligand ratios into the Cs-containing antisolvent in each well, as shown in Figure 1A. Here, we devised a modified LARP synthesis protocol to improve the reproducibility of the synthesis (see experimental procedures and Figures S1 and S2). Two pairs of surface ligands, oleic acid (OAc) with oleylamine (OLAm) and octanoic acid (OctAc) and octylamine (OctAm), are selected to explore the effect of the length and ratio of the ligand on the resulting PNCs. The precursor

[1]Institute for Advanced Materials and Manufacturing, Department of Materials Science and Engineering, The University of Tennessee Knoxville, Knoxville, TN 37996, USA

[2]Lead contact

*Correspondence: jyang70@utk.edu (J.Y.), mahmadi3@utk.edu (M.A.)

https://doi.org/10.1016/j.matt.2023.05.023

Please cite this article in press as: Sanchez et al., Understanding the ligand-assisted reprecipitation of $CsPbBr_3$ nanocrystals via high-throughput robotic synthesis approach, Matter (2023), https://doi.org/10.1016/j.matt.2023.05.023

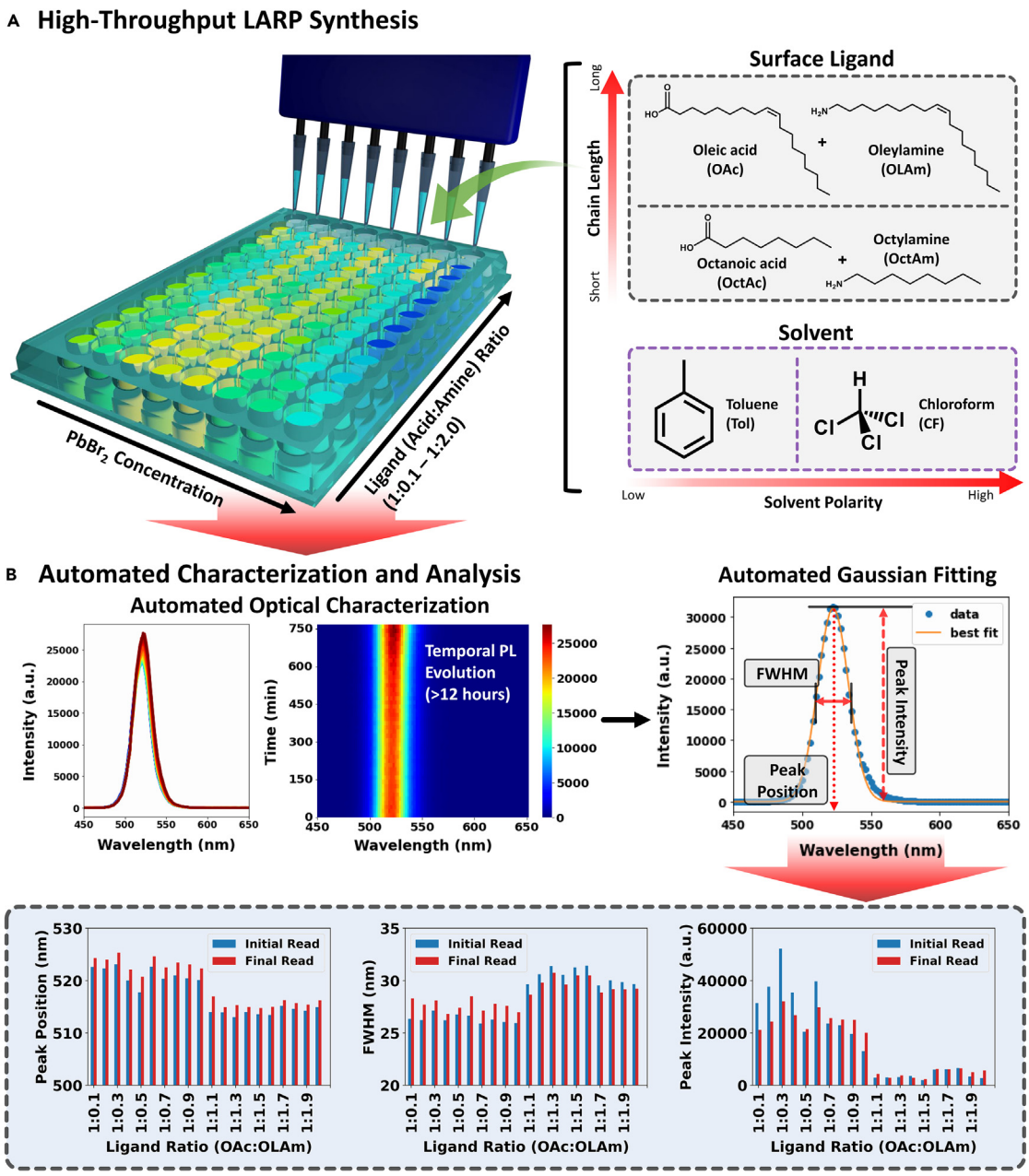

Figure 1. A workflow for high-throughput exploration of LARP synthesis of $CsPbBr_3$ PNCs

(A) Workflow for the high-throughput LARP synthesis of $CsPbBr_3$ nanocrystals with various ligand ratios, ligand pairs, and solvents.

(B) Automated characterization and analysis of the synthesized $CsPbBr_3$ nanocrystals.

solution is then injected into two different antisolvents with different polarities (i.e., toluene and chloroform; denoted as Tol and CF, respectively) to see the effect it may have on the formation of the $CsPbBr_3$ NCs. A detailed explanation of the high-throughput synthesis workflow can be found in the supplemental information.

After the synthesis of PNC, the well plate is subsequently transferred into a high-throughput optical reader, and the emission properties and colloidal stability of the PNCs are characterized by monitoring PL spectra for over 12 h. The underlying mechanisms within the compositions were then investigated by time-dependent PL,

Please cite this article in press as: Sanchez et al., Understanding the ligand-assisted reprecipitation of $CsPbBr_3$ nanocrystals via high-throughput robotic synthesis approach, Matter (2023), https://doi.org/10.1016/j.matt.2023.05.023

where the change of overall intensity, peak position, and full-width at half maximum (FWHM) are quickly traced through automated Gaussian fitting (Figure 1B). This overall experimental workflow provides rich data that give high-throughput insights into the optical properties, stability, and structural changes of the PNCs over time.

LARP synthesis of $CsPbBr_3$ PNCs is influenced by various factors including phase transitions, ligand binding, and degradation mechanisms. These can occur with variability of the synthesis parameters, all which correspondingly change the shapes, sizes, and size distributions of PNCs and the resulting PL spectra. Typically, the functional $CsPbBr_3$ NC with a nominal size of ~20 nm can be characterized by having a cubic structure, showing a green PL (peak at ~520 nm in PL spectrum).[6,29,30] The size of the PNCs can affect the position of the PL peak wavelength; it is expected that the larger the PNC size, the longer the (redshifted) PL peak wavelength.

The cubic $CsPbBr_3$ phase can be transformed to the hexagonal Cs-rich Cs_4PbBr_6, exhibiting insulator characteristics.[6,30,31] The $[PbBr_6]^{4-}$ octahedra become disintegrated from the $CsPbBr_3$ lattice, transforming to the hexagonal Cs-rich phase. The $[PbBr_6]^{4-}$ octahedra of Cs_4PbBr_6 are spatially isolated from each other in its lattice structure, thus creating a wide band gap of 3.9 eV.[6,30–32] Within the reaction system, the Cs_4PbBr_6 formation in turn consumes both Cs^+ and $[PbBr_6]^{4-}$ building blocks intended to be formed as $CsPbBr_3$, manifesting translucent solution and suppression of green PL with a larger FWHM.[27,33,34] Meanwhile, it is reported that excessive amines—by making Pb-amine complexes—would also induce the phase transformation from $CsPbBr_3$ to the Cs-rich Cs_4PbBr_6.[29,33,35] Together, the overall workflow proposed in this work based on a high-throughput robotic platform allows us to comprehensively understand the LARP synthesis of $CsPbBr_3$ PNCs, thereby rendering the overall synthesis landscape of the PNCs. Subsequently, this not only reveals the tendencies of structural changes or the thresholds for (undesired) phase transformations as functions of precursor concentrations and/or ligand ratios but also suggests an optimal synthetic condition to realize highly functional PNC ensembles.

As a preliminary study, the proposed workflow is implemented to explore the influence of overall ligand concentration in the precursor solutions before being injected into the Cs-containing antisolvent in a reaction well. Starting with a conventional ligand pair—OAc and OLAm—for the PNC synthesis, two ligand concentrations—1:15 and 1:30 v/v ratios between the ligand and $PbBr_2$ solution—are selected (Figure S3). The former ratio is comparable to the nominal ligand concentrations typically utilized for the LARP synthesis. From each PL spectrum with a ligand ratio, the resulting PL characteristics (i.e., peak positions, intensities, and FWHMs) at the specific time point (t = 0 and 12 h) are automatically extracted, as shown in Figure 2. In Figures 2A and 2B, the peak positions of the PNCs are within a similar wavelength range around ~515 nm. In fact, it has been reported that both the intact $CsPbBr_3$ PNCs and Cs_4PbBr_6 NCs where $CsPbBr_3$ PNCs are residually doped can emit green PL around 500 nm.[29,30,36,37,42,43] Therefore, the emergence of Cs-rich Cs_4PbBr_6 NCs is essentially not distinguishable from the PL spectra, particularly from the peak positions. However, the colorless dispersions in the well plate suggest the phase transformation to Cs_4PbBr_6 NCs (Figure S2).

The major differences in PL characteristics of these NCs are seen in their PL intensities and FWHMs (Figures 2C–2F). With increasing the concentration of amine in precursors, the significant intensity drops, and broadenings in PL peaks—a signature for the formation of Cs-rich NCs—are observed; excessive amine can react with Pb

Please cite this article in press as: Sanchez et al., Understanding the ligand-assisted reprecipitation of $CsPbBr_3$ nanocrystals via high-throughput robotic synthesis approach, Matter (2023), https://doi.org/10.1016/j.matt.2023.05.023

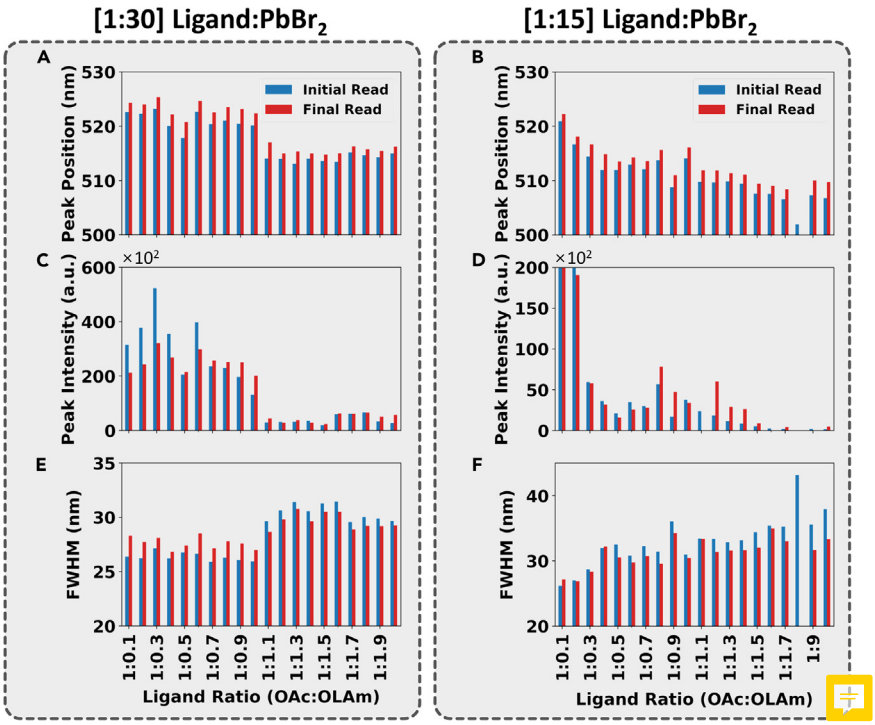

Figure 2. Automatically extracted PL characteristics of $CsPbBr_3$ PNCs synthesized with OAc:OLAm ligands in toluene

PL peak positions (A and B), peak intensities (C and D), and FWHMs (E and F), respectively. Two different volume ratios of ligand, i.e., OAc:$PbBr_2$ precursor solution (50 mM in DMF) are used: (A) 1:30 and (B) 1:15.

ions to form amine-Pb complexes, which cannot contribute to the formation of $CsPbBr_3$ PNCs but result in a Cs-rich Cs_4PbBr_6 phase.[33,38,39] Note that the drop in PL intensity and the widening of the FWHM are more apparent with higher ligand concentrations (i.e., 1:15, which is actually a nominal ligand concentration for LARP synthesis) for the PNC synthesis.[10–12]

The abrupt to gradual changes in the PL characteristics of PNCs with ligand:$PbBr_2$ ratios from 1:30 to 1:15 can be attributed to the relative increase in ligand concentrations with respect to the $PbBr_2$ precursor. The reduced amount of $PbBr_2$ increases the number of uncoordinated ligands in the precursor solutions that are ready to participate in PNC crystallization, while the ligands transform to ionic forms with an increase of the amine ratios. Due to the ionic nature of precursors and the dynamic diffusion of ligands in the solution,[26] the crystallization process can be described as a dynamic equilibrium of assembly and disintegration of inorganic precursors and ligands (i.e., $CsPbBr_3$-ligand $\leftrightarrows$ xCs + $y$$PbBr_2$ + uncoordinated ligands). The larger number of uncoordinated ligands could shift the chemical equilibrium to the left, according to Le Chatelier's principle, thereby retarding the disintegration process. This can subsequently retard the rate of phase transition from $CsPbBr_3$ to Cs_4PbBr_6, which is reflected as gradual changes in PL characteristics compared with those with higher $PbBr_2$ concentrations. A higher concentration of ligands (0.2–0.6 M depending on the added OLAm) than that of $PbBr_2$ (0.15 M of ions assuming a complete ion dissociation) in the precursor solutions could solvate the inorganic ions much more strongly, thereby disintegrating the crystallized inorganic nuclei and/or the premature PNCs. This might not only increase the chance for the

Please cite this article in press as: Sanchez et al., Understanding the ligand-assisted reprecipitation of $CsPbBr_3$ nanocrystals via high-throughput robotic synthesis approach, Matter (2023), https://doi.org/10.1016/j.matt.2023.05.023

formation of a Cs-rich phase rather than $CsPbBr_3$ but may also result in a larger size distribution, respectively mirrored as the lower PL intensities and larger FWHMs. Hereafter, the ligand:$PbBr_2$ ratio is fixed to 1:30 in this study, which provided better reproducibility and optical characteristics.

At an optimized OAc:OLAm ligand concentration, we see that when OAc is in the majority (i.e., OAc > OLAm), the synthesized PNCs exhibit longer PL wavelengths >520 nm, as shown in Figure 2A. They preserve fairly strong PL intensities (Figure 2C) and reasonable FWHM values around 26 nm (Figure 2E) even after 12 h. An increase of OLAm blueshifts the PL of the PNCs, which is an indication of a smaller NC. Meanwhile, the peak intensity is suppressed with larger FWHM values around 30 nm, speculating the emergence of Cs_4PbBr_6 NCs that would be attributed to Pb-amine complex formation.[33,38,39]

Further, the role of ligand chain length is investigated in our system, where we vary the ligand ratio of the 18 carbon OAc:OLAm and the ratio of the 8 carbon OctAc:OctAm ligands. The chain-length variations of the amines and acids were shown to have a correlation with the size and shape of NCs.[18,40–42] The extracted PL characteristics of $CsPbBr_3$ PNCs synthesized with OctAc:OctAm ligands are shown in Figures S4 and S5. A sudden blueshift in peak position occurs when the concentration of OctAm exceeds that of OctAc (Figure S5A), implying that the smaller sizes of NCs are synthesized at these conditions. Mixing of both OctAc and OctAm leads to proton transfer and, respectively, converts them to octanoate and octylammonium forms, which can participate in the PNC surface coordination. In OctAm-majority conditions, the excessive OctAm molecules cannot be protonated from the acid. Analogous to the observations in OAc:OLAm systems, these Lewis-base ligands could be responsible for the PL blueshifts; they attack the Pb and form the amine-Pb complexes, which prevent the precursor ion to grow the PNC larger.[43]

The peak intensity exhibits a lack of trend for the OctAc:OctAm ligands (Figure S5B), which is an indication that stable PNC formation may not be very favorable in this system; an increase or decrease in peak intensity over time may be due to the gradual PNC growth or complete decomposition of the PNC. As can be seen in Figure S5C, the FWHMs of the NCs are about ~27.5 nm when OctAc is in majority, and a slight increase in FWHMs of ~35 nm is observed when OctAm increases. The weaker the van der Waals (vdW) interaction among the shorter-chain ligands and the consequent smaller surface energy, the smaller ligand-confined reverse micelles (RMs) producing the PNCs with smaller surface-to-volume ratios tend to be form in the solution.[44] Meanwhile, these RMs would be relatively unstable in the polar reaction mixture system due to the larger portion of polar heads (i.e., carboxylate and ammonium) in the ligands (particularly the amine-excessive compositions) compared with the longer-chain ligand pairs. Thus, the synthesis of the PNCs is unlikely to be favorable in the OctAc:OctAm system.

The discrepancies in temporal PL changes of the PNCs prepared by different ligand pairs and ratios are also visualized in the PL spectra and spectro-temporal maps shown in Figure 3. It is immediately apparent that ligand type has an impact on the overall PL evolution; OAc:OLAm exhibits relatively little change in peak intensity and position over time (Figures 3A–3D), whereas OctAc:OctAm exhibits vast changes over time, expressing instability (Figures 3E–3H). These observations evidently infer that ligand chain length not only influences the dimensionality but also the long-term colloidal stability of the resulting $CsPbBr_3$ PNCs. Note that, in

Please cite this article in press as: Sanchez et al., Understanding the ligand-assisted reprecipitation of $CsPbBr_3$ nanocrystals via high-throughput robotic synthesis approach, Matter (2023), https://doi.org/10.1016/j.matt.2023.05.023

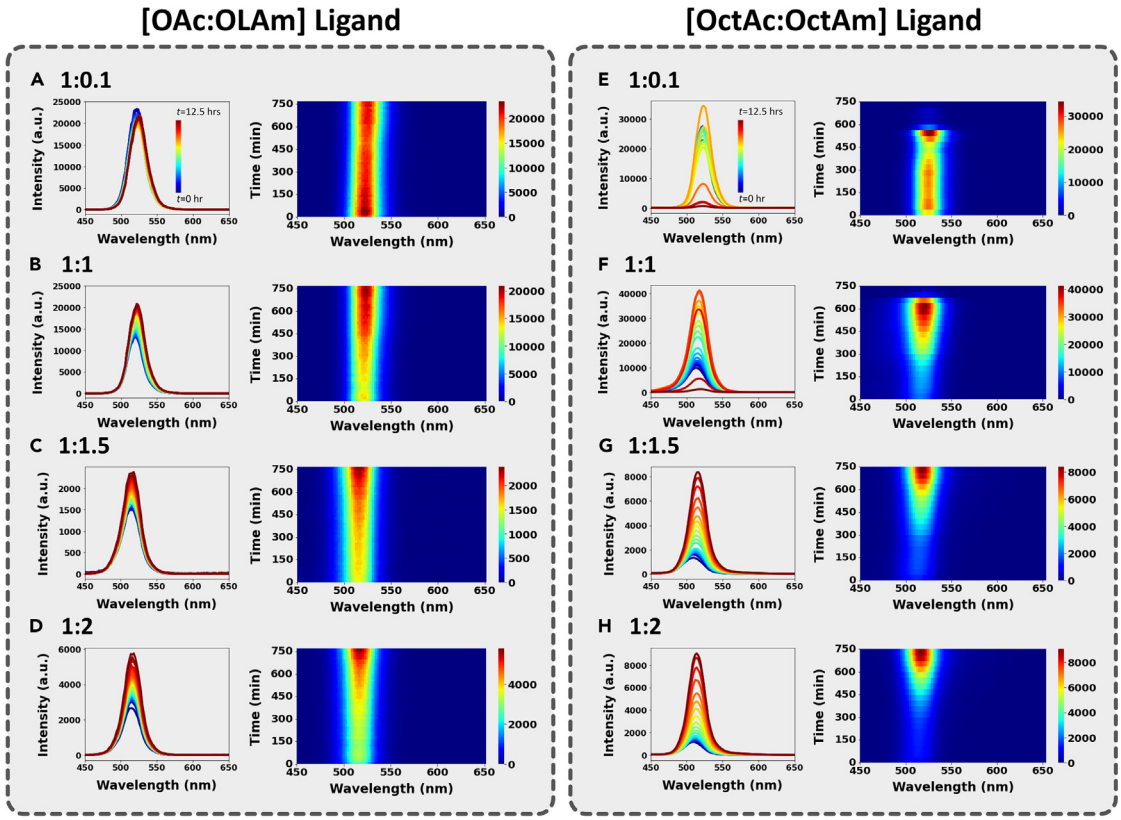

Figure 3. Time-dependent PL spectra and corresponding heatmaps of $CsPbBr_3$ PNCs with various ligand ratios

1:0.1 OAc/OLAm in toluene (A); 1:1 OAc/OLAm in toluene (B); 1:1.5 OAc/OLAm in toluene (C); 1:2 OAc/OLAm in toluene (D), respectively; 1:0.1 OctAc/OctAm in toluene (E); 1:1 OctAc/OctAm in toluene (F); 1:1.5 OctAc/OctAm in toluene (G); and 1:2 OctAc/OctAm in toluene (H), respectively.

PNC dispersion, the binding of the carboxylate and ammonium ligands is described as a dynamic equilibrium, where the ligands are simultaneously attached and detached at the PNC surface.[27] Given the smaller molecular weight of OctAc and OctAm, more dynamic adsorption/desorption of the ligands (i.e., faster reaction rates) can be anticipated. In turn, this could crucially compromise the colloidal stability of the PNC dispersions, in accordance with our observations. It should be noted that, here, from the overall synthesis batches using toluene, we could not observe any notable PL emissions centered <500 nm during LARP synthesis. Those emissions are typically observed from the low-dimensional $CsPbBr_3$ polymorphs (such as nanoplatelets) exhibiting a strong quantum confinement effect.[45–48] Thus, these observations suggest that our synthesis protocol, at the given experimental conditions, mainly produces cubic PNCs rather than such low-dimensional $CsPbBr_3$ nanostructures. It is reported that the use of polar solvents, additives, or amine-poor ligand systems can promote the nucleation and growth of nanoplatelet forms.[45,47]

To examine the reproducibility of our LARP-synthesis protocol from the microscale to a larger scale (10 mL), we synthesized PNCs with selected ligand ratios of 1:0.1, 1:1, 1:1.5, and 1:2 for both the OAc:OLAm and OctAc:OctAm ligand systems. Figure S6 exhibits photos of emitting PNC dispersions in 10 mL volume scale synthesized with different ligand ratios and ligand pairs, showing pale green colors for amine-rich conditions in both ligand systems. In addition, we compared the PL emission behaviors of PNCs synthesized manually (larger scale) and by robot

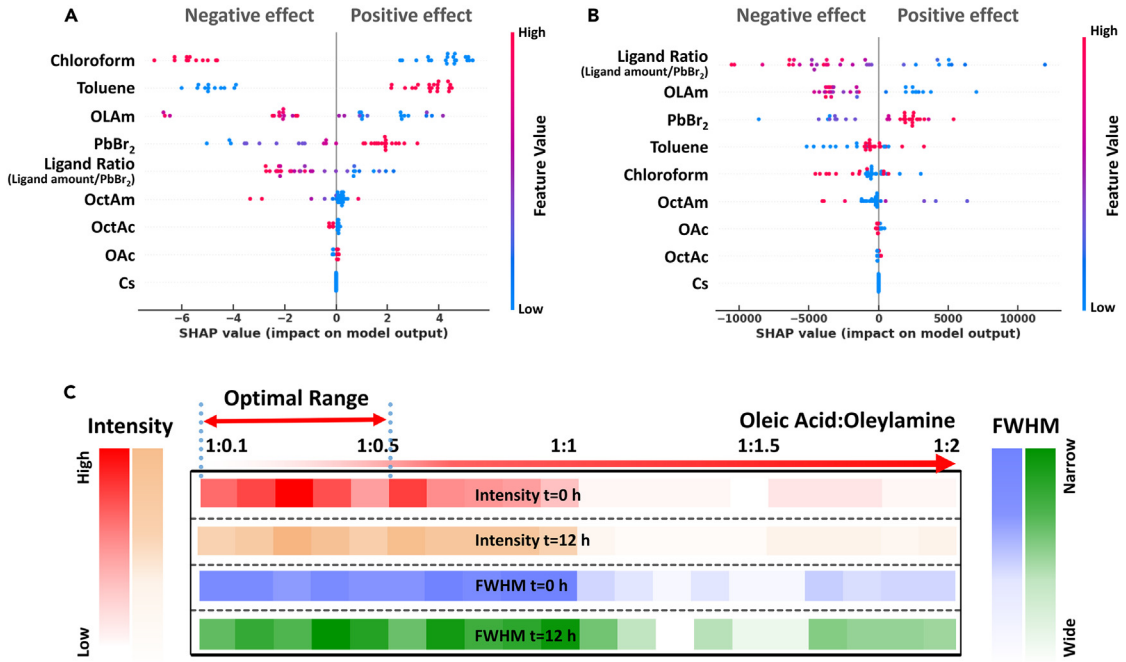

Figure 4. SHAP plot analysis and assessment of synthesis features impact

(A and B) SHAP plot with rating the impact of each feature value on (A) peak position and (B) peak intensity.

(C) The assessment of OAc/OLAm ligand ratio impact on PL intensity and FWHM over time.

(smaller scale), which showed consistent emission characteristics. This not only justifies the reproducibility of the devised synthesis method but also guarantees that our high-throughput observations can be transferred to large-scale synthesis.

To provide a detailed examination of the impact of various parameters (e.g. ligand ratio:$PbBr_2$, ligand chain length, and the antisolvent polarity) on the formation of $CsPbBr_3$ PNCs and Cs-rich NCs, we utilized the machine learning method "Shapley additive explanations (SHAP)." SHAP is a powerful tool that can assign a positive or negative impact to each parameter on the overall prediction of the system.[49–51] We trained four distinct models, including linear regression, random forest regression, support vector machine, and neural network, to understand the patterns within the peak position change. The root-mean-square error (RMSE) was computed for each model to measure the average difference between the predicted values and the actual values of peak position (Figure S7). We found that the random forest regression model is the best-performing model due to its robustness to outliers and noisy data, ability to model non-linear relationships, and capacity to measure feature importance.[52,53] The random forest regression model randomly samples the input feature variables at each tree split, and SHAP then computes the contribution of each feature to the prediction by considering all features and their interactions.

We utilized the random forest regression model to assess the PL peak position and peak intensity. SHAP is then used to rank the importance of each parameter. Our analyses reveal that chloroform has a negative impact, resulting in a blueshifted peak position when a large amount of chloroform is used, while toluene has a positive impact, leading to a PL redshifted peak position with an increase of the volume of toluene (Figure 4A). OLAm, $PbBr_2$, and ligand ratio:$PbBr_2$ are found to be crucial factors, with a lower amount of OLAm being most beneficial for red shifting the peak

Please cite this article in press as: Sanchez et al., Understanding the ligand-assisted reprecipitation of $CsPbBr_3$ nanocrystals via high-throughput robotic synthesis approach, Matter (2023), https://doi.org/10.1016/j.matt.2023.05.023

position, a higher amount of $PbBr_2$ contributing to a considerable redshift in peak position, and a lower addition of ligand ratio to $PbBr_2$ also having positive impact. OctAm, OctAc, OAc, and Cs have the least or no impact on the model, possibly due to the lack of parameter variability in the model.

Furthermore, we utilized SHAP to evaluate the impact of each parameter on the PL peak intensity (Figure 4B). The ligand ratio:$PbBr_2$, OLAm, and $PbBr_2$ are rated as the top three most impactful features. A low amount of ligand ratio and OLAm is found to be beneficial in contributing to a higher peak intensity (positive impact), and a higher amount of $PbBr_2$ also has a positive impact on the model. Toluene, chloroform, and OctAm all have a low impact on positive peak intensity contribution and actually provided a stronger negative impact (decrease in PL intensity) regardless of the amount used. Finally, OAc, OctAc, and Cs have little to no impact on peak intensity, which may be attributed to the lack of parameter variability in the synthesis parameters. Overall, our findings provide a comprehensive analysis of the impact of various parameters on the formation of $CsPbBr_3$ PNCs and Cs-rich NCs, highlighting the utility of SHAP in understanding the underlying factors influencing the system.

Based on the comprehensive PL analysis of the synthesized PNCs and machine learning-based parametric assessments, a summarized map of the intensity and FWHM for the various ligand ratios of OAc:OLAm is depicted in Figure 4C. This can clearly reveal the global trends in PNC functionalities, thereby allowing us to identify the best ligand ratio that provides better stability in ambient conditions over time. The map is divided into lighter and darker regions, with the lighter regions indicating low intensity or broad FWHM, indicating poor stability of the PNC. On the other hand, the darker regions indicate either the highest intensity or the narrowest FWHM, suggesting the appropriate ligand ratio for the best stability of PNCs over time. After careful consideration, the optimal range to produce stable PNCs is between 1:0.1 to 1:0.5 OAc:OLAm. This decision is made based on the majority of PNCs in this range having little to no change in peak intensity and FWHM, resulting in the highest PL peak intensity and narrowest FWHM. In accordance with our observations, OAc:OLAm ligand ratios of 1:1 and above lead to the lowest PL peak intensity and broad FWHM.

In continuation of exploring the role of ligand chain length on the morphology and stability of $CsPbBr_3$ NCs, transmission electron microscopy (TEM) analysis was conducted, and the images of PNCs synthesized with OAc and OLAm are shown in Figures 5A–5D (the corresponding particle size distribution histograms are shown in Figure S8). In Figure 5A, the TEM image of NCs with a 1:0.1 ratio of OAc:OLAm are cubic and monodispered, with an average particle length of 10 nm. In Figure 5B, the NCs exhibit a slight decrease in size (~7 nm) yet maintain a state of monodispersity. In Figure 5C, the ligand ratio is 1:1.5, and OLAm is in the majority here. We can see the presence of ellipsoidal-spherical nanoparticles (NPs) with a nominal size ~119 nm. These NPs are a combination of cubic and hexagonal NCs together,[54] most likely in the transition to the Cs-rich NCs. In Figure 5D, the ligand ratio of 1:2 OAc:OLAm shows mostly hexagonal, aggregated NPs. In addition, we observe a variety of NPs including circular or oblong NPs with an average size of 114 nm. The hexagonal-shaped features are likely the Cs-rich Cs_4PbBr_6 NCs.[54] The aggregation of these NCs is most likely due to the lack of OAc found in the system. This is because OAc is known to regulate the aggregation of NPs, while OLAm is known to control their sizes.[25–27] It is demonstrated that OLAm is facilitating the decomposition process of $CsPbBr_3$ into Cs_4PbBr_6.

Please cite this article in press as: Sanchez et al., Understanding the ligand-assisted reprecipitation of $CsPbBr_3$ nanocrystals via high-throughput robotic synthesis approach, Matter (2023), https://doi.org/10.1016/j.matt.2023.05.023

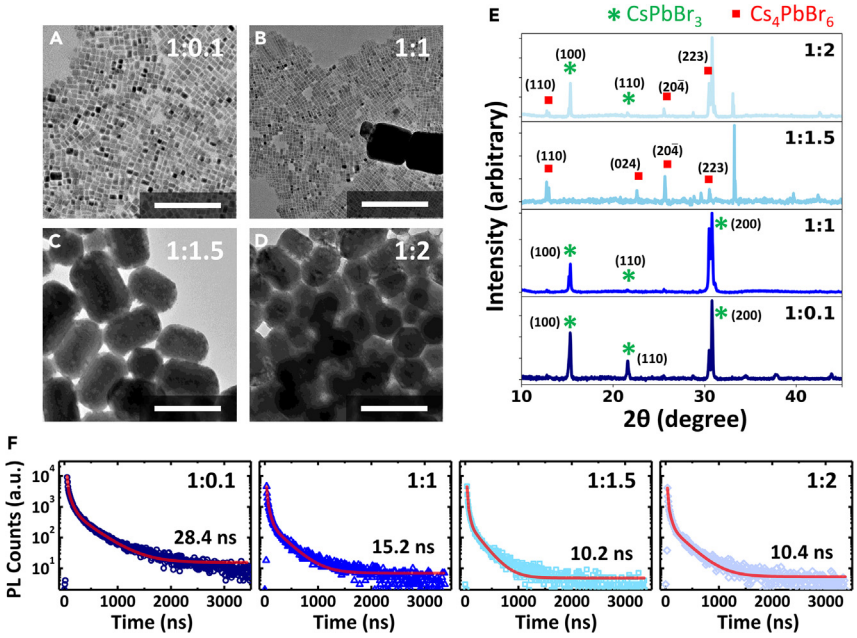

Figure 5. Selected-batch characterizations of $CsPbBr_3$ PNCs

(A–D) TEM images of $CsPbBr_3$ PNCs prepared with OAc/OLAm in toluene with ratios of (A) 1:0.1, (B) 1:1, (C) 1:1.5, and (D) 1:2, respectively. Scale bar: 200 nm.

(E) XRD patterns of the corresponding PNCs. Green asterisks and red squares respectively associated with the crystal lattices of $CsPbBr_3$ and Cs_4PbBr_6 are marked.

(F) TRPL decay curves of the corresponding PNC dispersions.

TEM images of $CsPbBr_3$ PNCs synthesized with OctAc:OctAm (at ligand ratios of 1:0.1 and 1:1) were also collected (Figure S9). At a 1:0.1 (OctAc:OctAm) ratio, considerable amounts of PNCs were aggregated or even fused with each other, thereby rendering various sizes as shown in Figure S9A. The shorter-chained ligands are not effective to produce monodispersed cubic $CsPbBr_3$ PNCs, analogous to the observations in $CsPbI_3$ PNCs using a short ligand that provides a weak vdW force.[24] Increasing the amine concentration (1:1) shows the co-existence of smaller particles and giant hexagonal-shaped particles as seen in Figure S9B. The smaller PNCs can be attributed to the poor binding ability of OctAc:OctAm due to their smaller molecular weights, as speculated by their poor temporal PL stabilities (Figure 3E–3H).[27] The formation of these giant NPs is likely attributed to the formation of Cs-rich Cs_4PbBr_6 NCs,[39,54] together with the Ostwald ripening.[55] We should note that from the TEM images, we could not find any features of low-dimensional $CsPbBr_3$ polymorphs,[45–48] corroborating our hypothesis from PL observations that those phases are not the product of our LARP-synthesis protocol.

Corresponding X-ray diffraction (XRD) patterns of the $CsPbBr_3$ PNCs synthesized with OAc:OLAm ligands are shown in Figure 5E. We can see that when OAc is in the majority, the $CsPbBr_3$ phase is confirmed to be the only phase present. The $CsPbBr_3$ crystal structure was confirmed to be orthorhombic (*Pbnm*), with peak positions at 15.3, 21.6, and 30.8° corresponding to (100), (110), and (200) facets, respectively. When the amount of OLAm is increased, we observe the co-existence of $CsPbBr_3$ and Cs_4PbBr_6 phases as indicated in the XRD pattern, notably with peak positions at 12.6, 25.3, and 30.5°, which correspond to (110), (20$\bar{4}$), and (223) facets, respectively. The emergence of a Cs-rich phase agrees with the suppression of PL intensity, a blue shift, and the widening of the FWHM due to the insulator-like effect

Please cite this article in press as: Sanchez et al., Understanding the ligand-assisted reprecipitation of $CsPbBr_3$ nanocrystals via high-throughput robotic synthesis approach, Matter (2023), https://doi.org/10.1016/j.matt.2023.05.023

of Cs_4PbBr_6.[33,38,39] The XRD results also agree with the TEM images that exhibit $CsPbBr_3$ NCs when OAc is in the majority.[38,56,57] Here, the trend between ligand ratios has become abundantly clear, so investigation of other parameters affecting the NCs is important in understanding all the changes that can occur. The stronger $CsPbBr_3$ diffraction peaks are observed from the PNCs synthesized with a 1:2 acid:amine ratio compared with those with a 1:1.5 ligand ratio. This could be attributed to the increased chemical complexity of the precursor, which contains both fully protonated ionic ligand pairs and excessive (unprotonated) amines. This could promote uncontrollable crystallization of both species where the relatively larger $CsPbBr_3$ crystallites are doped into the Cs-rich phase as a consequence, considering the absence of cubic $CsPbBr_3$ PNCs at the 1:2 ligand ratio in the corresponding TEM image (Figure 5D).

Additionally, the photophysical properties of the synthesized $CsPbBr_3$ PNCs with selected OAc:OLAm ligand ratios are investigated using time-resolved PL (TRPL) spectroscopy (Figure 5F; Table S1). Our results show that PNCs synthesized with carboxylic acid-rich ligands exhibit larger average PL lifetimes compared with those synthesized with amine-rich ligands. This observation indicates a reduction in surface defects and suppressed non-radiative recombination pathways. However, an increase in the amount of OLAm in the system, particularly at the amine-rich conditions, leads to shorter PL lifetimes by the promotion of non-radiative recombination, attributed to an increase in surface defects. These observations are in agreement with steady-state PL behaviors (Figure 2), where the amine-rich PNCs exhibit weak and blueshifted photon emission. It is likely that the dynamic chemical actions[26] taking place in the amine-rich precursors not only cause uncontrollable multi-phase formation but also notably result in defective surface-promoting non-radiative recombination. Overall, these findings suggest that the appropriate ratio of OAc:OLAm is crucial in optimizing the radiative properties of these PNCs, where the carboxylic acid-rich conditions are necessary to obtain emissive PNCs.

We attempted to trace the ionic form of $PbBr_2$ in precursor solution with the ligands. However, the absorption range of the $PbBr_2$-based ionic complexes is out of the detection range (Figure S10). Alternatively, we monitored the absorption spectra of the PbI_2 ionic complexes in solution as a function of OAc:OAm ratio and OctAc:OctAm (Figure S11). We observe two distinctive peaks at 280 and 320 nm upon addition of pure OAc, respectively assigned to be positive-charged $[PbI]^+$ and charge-neutral $[PbI_2]$ complexes.[58,59] With increasing OLAm molar ratios, the $[PbI_2]$ peak reduced and disappeared, suggesting that polar $[PbI]^+$ species are dominant in the precursor system by increasing the OLAm molar ratio (Figure S11A). A similar trend occurs with OctAc:OctAm ligands where there is a distinct peak at 320 nm upon the addition of pure OctAc. The 320 nm peak can be assigned to the charge-neutral $[PbI_2]$ complex. With the addition of OLAm molar ratios, the $[PbI_2]$ peak reduces and disappears, suggesting that the charge-neutral $[PbI_2]$ complex becomes less dominant in the system as the polar species becomes more dominant (Figure S11B). This could cause the faster diffusion of the precursors in a reaction system and the PNC formation to be more dynamic,[60] resulting in poorer PNCs with broader size distributions as seen from the OctAc:OctAm cases.

Interaction of ligand with solvent is not only crucial for the colloidal stability of the PNCs but is also a determinant factor in their synthesis; it can influence the optoelectronic properties and phase developments of the resulting PNCs. Recall the ionic nature of the PNC lattice bonding, which therefore requires the polar and ionic heads (i.e., carboxylates and ammoniums) for ligand surface coordination. Polar

Please cite this article in press as: Sanchez et al., Understanding the ligand-assisted reprecipitation of $CsPbBr_3$ nanocrystals via high-throughput robotic synthesis approach, Matter (2023), https://doi.org/10.1016/j.matt.2023.05.023

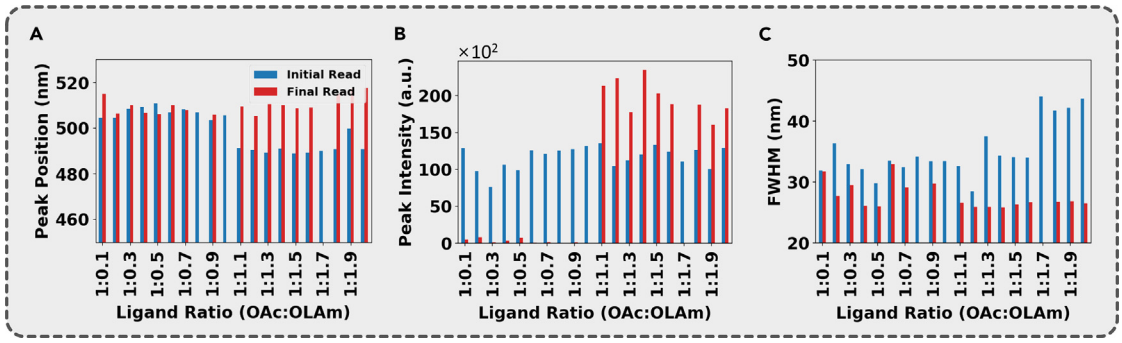

Figure 6. Automatically extracted PL characteristics of $CsPbBr_3$ PNCs synthesized with OAc/OLAm ligands (1:30 v/v% vs. $PbBr_2$ solution) in chloroform

PL peak positions (A), peak intensities (B), and FWHMs (C), respectively.

solvents can strongly interact with such ionic ligands (i.e., attraction), thus leading to their solvation—a competitive process with ligand binding onto the PNC surface—being more feasible at the end.[18] As a consequence, the more polar solvent rendering stronger ligand-solvent interaction is used, the more likely the NCs lose their colloidal and structural integrity; indeed, faster diffusion of OAc in $CDCl_3$ compared with Tol-d_8 was evidenced by diffusion-ordered nuclear magnetic resonance spectroscopy.[61] This subsequently leads to different morphologies and crystal phases over time. In light of this, next, the effect of solvent on PNC synthesis is evaluated. We explore the PL characteristics of $CsPbBr_3$ PNCs synthesized in chloroform—which is more polar than toluene—as a solvent, as seen in Figure 6. Although both are considered non-polar solvents, chloroform is more polar than toluene, as is known by their different dielectric constants and polarity indices (2.38 and 2.4 for toluene and 4.81 and 4.1 for chloroform, respectively).[62,63]

The role of the ligand ratio paired with different polarity of solvents and its effect on the stability of the PNCs is also investigated by monitoring PL evolutions (Figure S12). In Figure 6A, the PL peak positions exhibit at shorter wavelengths (around 500 nm) than those from toluene (around 520 nm) and undergo blueshifts with increasing OLAm. The PNCs exhibit nominal PL intensities at the initial stage but show different tendencies, respectively, depending on the OAc or OLAm majority in ligand compositions after 12 h (Figure 6B). In OAc majorities, the PL intensities are largely suppressed, whereas notable increases are observed in OLAm majorities. Meanwhile, there is a broadening tendency in FWHMs with an increase of OLAm at the initial stage but no appreciable differences, particularly after 12 h (Figure 6C). In the OctAc/OctAm system, the PL peaks initially emerged, but they rapidly disappeared, thereby showing no characteristic tendencies in PL properties (Figures S4 and S13). This indicates extremely poor colloidal stability of the resulting PNCs in CF environment.

The ligands in the former cases (i.e., OAc majorities) are present in ionic forms, which are prone to be influenced by polar solvent. The enhanced strength in a ligand-solvent interaction can shift the equilibrium of ligand binding at the PNC surface toward detachments, gradually causing PNC decomposition; the fragmented PNC features in the TEM image (Figure S14A) corroborate this. As a consequence, the emission features of the PNCs become greatly suppressed. Though the PL intensities were increased in the OLAm-majority regime, we observe the giant hexagonal-shaped NPs even at the 1:1 ligand ratio (Figure S14B) by its decomposition. This suggests that rather than forming an ensemble where the $CsPbBr_3$ PNCs are dominant,

Please cite this article in press as: Sanchez et al., Understanding the ligand-assisted reprecipitation of $CsPbBr_3$ nanocrystals via high-throughput robotic synthesis approach, Matter (2023), https://doi.org/10.1016/j.matt.2023.05.023

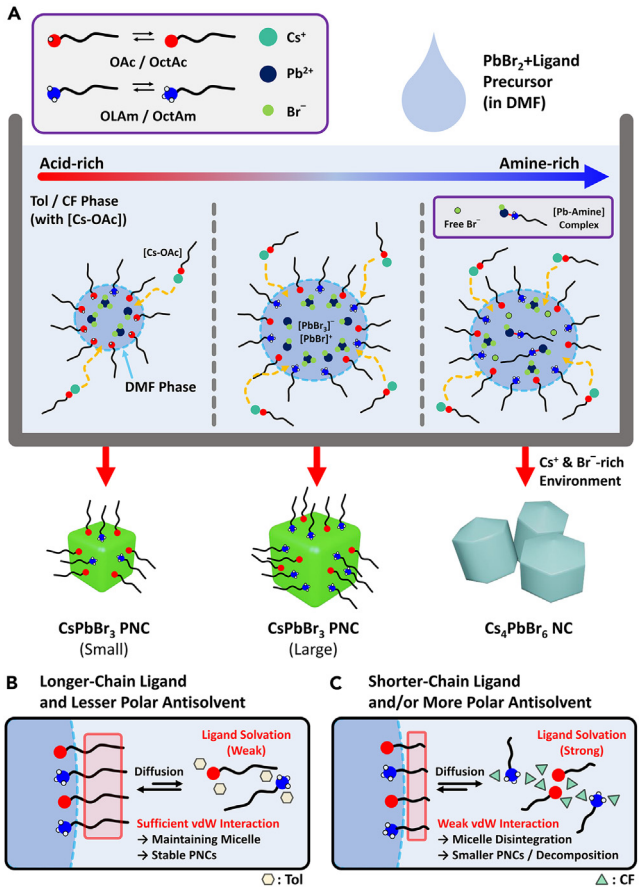

Figure 7. Mechanistic insights of LARP synthesis of $CsPbBr_3$ PNCs

Schematic description of reverse micelle formation behaviors and ligand behaviors during LARP process in synthesizing $CsPbBr_3$ PNCs.

(A) Description of reverse micelle (RM) formation behaviors during LARP process as a function of ligand ratio, which determines the final PNC structures. Schematic scenarios describing ligand behaviors at RM interfaces.

(B and C) Long-chain ligand and less-polar antisolvent (OAc/OLAm-toluene) (B) and short-chain ligand and more-polar antisolvent (OctAc/OctAm-chloroform) (C).

formation of Cs_4PbBr_6 NCs is favored due to the unprotonated amines as seen in Figure 5. Given the strong PL intensity and the moderate FWHMs of ~25 nm, a plausible scenario to describe the feature is the integration of small $CsPbBr_3$ PNCs with the Cs_4PbBr_6 NCs during the gradual reaction for 12 h as previously observed.[13,39–43]

From our observation, a generalized chemical reaction associated with the LARP process, as a function of the carboxylic acid/amine ligand ratio, can be described with infinitesimal RM models that are formed in a reaction system, as proposed in Figure 7A. Upon injection of the precursor solution (DMF phase), intuitively, the instant formation of ligand RMs at the infinitesimal DMF/solvent (Tol or CF) interface can be envisaged, where the ligand heads confine the inorganic $PbBr_2$—both in neutral [$PbBr_2$] and ionic $[PbBr_3]^-/[PbBr]^+$ forms—inside the RM. Then, the Cs-oleates dissolved in the solvent phase are introduced into the RMs, initiating the crystallization of the $CsPbBr_3$ lattice. The ligands at the RM interface can subsequently coordinate to the lattice surface, thereby producing dimensionally confined colloidal PNCs.

Please cite this article in press as: Sanchez et al., Understanding the ligand-assisted reprecipitation of $CsPbBr_3$ nanocrystals via high-throughput robotic synthesis approach, Matter (2023), https://doi.org/10.1016/j.matt.2023.05.023

Carboxylic acids are used to prevent coagulation of NPs due to their steric repulsion[18] and decrease halogen vacancies that can be found on the surface of $CsPbBr_3$ PNCs,[64] while amines are used to control the crystallization, thus controlling the size of NCs.[42,65] At the carboxylic acid-rich regime (i.e., acid > amine), the smaller amounts of ligands could render a smaller RM size, producing smaller PNCs. With increasing the amines, primarily based on the increased amounts of the ligands in the system, larger RMs can be formed, which results in the larger PNCs. Note that the increase of amine also results in an increase of the ionic $PbBr_2$ species, as seen from absorption spectra of the precursor solutions (Figure S10). These ionic forms accelerate $CsPbBr_3$ crystallization,[44] which can result in PNCs with larger defect densities; this is likely responsible for the decrease of PL intensity observed from the PNCs with the OAc:OLAm ratio of 1:0.5–1:1 (Figure 1).

To gain further insights into the chemical nature of precursor systems, Fourier transform infrared (FTIR) spectroscopy is conducted. As shown in Figure S15, in both precursor solutions with different ligand pairs, at the acid:amine ratio of 1:0.1, an upshift of C=O stretching modes from those of the corresponding neat ligand systems (1,723 from 1,707 cm^{-1} and 1,724 from 1,705 cm^{-1} for OAc:OLAm and OctAc:OctAm systems, respectively; Figures S15A–S15D) is observed. Additionally, the C-O-H bending mode at ~1,412 cm^{-1} can be observed in both cases for this ligand ratio. These observations indicate that the charge-neutral carboxylic acids are coordinated with $PbBr_2$ in both ligand systems. Meanwhile, a peak at 1,641 or 1,644 cm^{-1} is observed that is distinctive from the DMF C=O stretching peak (1,679 cm^{-1}), which is assigned to be an upshifted NH_3^+ stretching mode of OLAm and OctAm (Figures S15C and S15D),[66] respectively, as a result of proton transfer from carboxylic acid. This suggests that ammoniums interact with precursor species (particularly $PbBr_3^-$). With increasing the ratio of amine, a broad FTIR band centered at 1,553 cm^{-1} emerges in both ligand pair systems. This is likely attributed to the overlap of asymmetric COO^- and NH_3^+ stretching modes,[66,67] which strongly interact with each other and DMF solvent via hydrogen bonding,[68] rather than solvating the $PbBr_2$. It is known that the ionic forms of the ligands are beneficial to colloidal stability and emission behaviors of the PNCs, as they can passivate surface defects in the ionic lattice.[23,69,70] However, the FTIR observations suggest that, for nucleation in the LARP crystallization process, acid-rich conditions with more charge-neutral carboxylic acid ligands are advantageous to control the crystallization process,[60] thereby producing stable and emissive PNCs. This is confirmed by insignificant temporal PL changes of PNCs synthesized by acid-rich conditions (Figures 2A and S3). Due to the dynamic changes in the temporal PL characteristics of PNCs synthesized under amine-rich conditions (Figure 2) and the dynamic binding nature of ligands on the PNC surface,[26] it is likely that the ligands in ionic forms continuously disintegrate and reconstruct the PNC lattices with larger defect densities during the crystallization process.

At the amine-rich regime, Pb-amine complex formation is expected.[37,43] This not only compromises the number of active Pb^{2+} to make $CsPbBr_3$ but also releases free Br anions. Subsequently, a Cs^+- and Br^--rich condition is manifested, promoting the formation of Cs-rich Cs_4PbBr_6 NCs rather than the originally intended $CsPbBr_3$ PNCs. Note that the reactivity of the amine is larger for OctAm than OLAm given its dipole moment (Figure S16) estimated from *ab initio* calculations, rationalizing the promoted formation of the giant of Cs_4PbBr_6 NCs observed at a 1:1 OctAc:OctAm ratio (Figure S14B).

Please cite this article in press as: Sanchez et al., Understanding the ligand-assisted reprecipitation of $CsPbBr_3$ nanocrystals via high-throughput robotic synthesis approach, Matter (2023), https://doi.org/10.1016/j.matt.2023.05.023

The vdW interaction of ligand plays a crucial role in PNC synthesis. Larger ligands with longer alkyl chains provide stronger vdW interactions (i.e., inter-chain attraction) with each other.[38] This renders a more rigid RM interface for desired PNC growths where the ligand solvation and the consequent disassembly of RM is largely mediated under a weakly polar solvent system. In contrast, the use of shorter-chain ligands or polar solvents could significantly compromise the rigidity of the RMs and release the ligands to be solvated.[18,61] As a consequence, poor-shaped PNCs can be obtained.

Through a detailed examination of the PL variability and TEM and XRD characterizations of the synthesized PNCs, we have described the formation behaviors as a function of the ligand ratio in Figure 7A. The gradual increase of amine in the system leads to the growth of $CsPbBr_3$ PNCs, eventually leading to a phase transition into Cs-rich NCs. Additionally, we have determined that the chain length and polarity of the antisolvent influence the functionality and structure of the PNCs, as the ionic diffusion of the ligands plays a vital role in the formation of PNCs (Figure 7B). It is worth noting that the optimally synthesized PNCs (i.e., 1:0.1 OAc:OLAm) maintained the original PL features over 12 h without any purification process, despite the use of DMF as a precursor solvent—which is known to be deleterious for PNC stability. This infers that, counterintuitively, the physicochemical nature of antisolvent more crucially determines the PNC stability.

Note that the crucial chemical parameters describing the overall LARP crystallization process, such as antisolvents, ligand types, and ratios, are also highly ranked upon SHAP assessments. As an example, SHAP analysis clearly identifies that the more-polar antisolvent (i.e., chloroform) can negatively impact the synthesis sequence to obtain the green-emitting $CsPbBr_3$ PNCs, and vice versa for its less-polar counterpart (i.e., toluene), as shown in Figure 4A. The SHAP analysis results clearly visualize the magnitude of each contribution for all chemical parameters in PNC synthesis, which is difficult to realize by individual analysis. Moreover, the consistency of the trends with manual interpretations strongly support our proposed mechanisms for LARP crystallization process. As a result, this comprehensive exploration provides insights into optimized process designs for the synthesis of high-performance PNCs.

Overall, our results highlight the critical role of ligand properties, ligand ratios, and antisolvent properties in the synthesis of PNCs using the LARP method. The high-throughput PL exploration proposes an effective way to formulate PNC formation dynamics in parametric spaces, which are tightly entangled with each other. Note that state-of-the-art synthesis routes for high-quality PNCs are devised via judicious ligand selections.[60,71] Together with these insights, the workflow demonstrated in this study is a powerful tool to construct a detailed chemical map of PNC synthesis, for bespoke tailoring of their functionalities.

Conclusion

In this study, we have executed a high-throughput automated synthesis platform to accelerate the investigation of growth and stability of LARP-synthesized PNCs under various conditions. By using two different acid-base pairs—OAc:OLAm and OctAc:OctAm—we conducted a systematic analysis of the impact of ligand properties, such as chain length, concentration, and ratio, on the growth and functionality of $CsPbBr_3$ NCs. Combined with ML-based parametric assessment, our findings revealed that the use of short-chain ligands (i.e., OctAc:OctAm) and/or polar antisolvents (i.e., CF) results in the production of non-functional PNCs with poor size, shape, and stability. On the other hand, the incorporation of longer-chain ligands

produces stable and homogeneous PNCs. However, the use of excessive amines led to the formation of a Cs-rich non-perovskite structure characterized by larger size distributions and impaired emission functionality. This suggests that the ionic diffusion of the ligands within the system plays a critical role in determining the structure and functionality of the PNCs. Our high-throughput approach provides a firsthand, detailed guide for the synthesis of desired PNCs using the LARP method.

EXPERIMENTAL PROCEDURES

Resource availability

Lead contact

Further information and requests for resources should be directed to the lead contact, Mahshid Ahmadi (mahmadi3@utk.edu).

Materials availability

All materials generated in this study are available from the lead contact.

Data and code availability

All original code is available in this paper's supplemental information. The code for data analysis can be found on the following GitHub link: https://github.com/SLKS99/Understanding-the-Ligand-Assisted-Reprecipitation-of-CsPbBr3-Perovskite-Nanocrystals-via-High-Throug.

Materials

Cesium carbonate (Sigma-Aldrich, ReagentPlus 99%), lead bromide (Sigma-Aldrich, 99.999% trace metals basis), OAc (Sigma-Aldrich, technical grade, 90%), OLAm (Sigma-Aldrich, technical grade, 70%), OctAc (Alfa Aesar, 98+%), OctAm (Alfa Aesar, 98+%), toluene (Sigma-Aldrich, anhydrous, 99.8%), and chloroform (Sigma-Aldrich, anhydrous >99%, contains 0.5–1% ethanol as a stabilizer) were used. No further purification was done.

Precursor synthesis

200 μL OAc was added into a vial with 0.0163 g cesium carbonate. 20 mL toluene was added into the vial and left to stir for about an hour until dissolved. 0.184 g $PbBr_2$ was dissolved in 10 mL DMF and left to stir for about an hour. The same steps were done for the synthesis of Cs-OctAc but instead of 200 μL OAc, 200 μL OctAc was used.

PL measurements

PL spectroscopy was obtained using the Biotek Cytation 5 Hybrid Multi-Mode Reader. The excitation was set to 365 nm, and the emission was measured over a range of 400–650 nm with a step of 2 nm. The measurement occurred 7 mm below the bottom of the well plate and was performed in sweep mode. The measurement was repeated every 10 min for approximately 12 h.

Characterizations

Absorption spectra of the precursor solutions were collected using the Biotek Cytation 5 Hybrid Multi-Mode Reader. All TEM images were taken on the Zeiss Libra 200 MC. The PNCs were drop casted onto a TEM copper grid (200 mesh) coated with carbon formvar and left to dry over a filter for approximately a minute before loading. A 200 kV accelerated e-beam was used for characterizations. XRD patterns were collected by using a high-resolution X-ray diffractometer (Malvern Panalytical Empyrean). The synthesized PNCs were drop casted onto a precleaned Si wafer and vacuum dried prior to mounting to the measurement stage. FTIR spectra were

collected by using a Nicolet iS50 FTIR (Thermo Scientific) spectrometer. TRPL dynamics were collected by using PL in the dynamic regimes measured by the SPEX Fluorolog 3 spectrometer. The TR photoexcitation source was from a pulsed laser beam (343 nm, 4 mW) generated through a harmonic generator (Ultrafast Systems, second harmonic) with a Pharos laser (Light Conversion, 100 kHz, 1,025 nm, 290 fs).

Calculation details of dipole moment of amine and ammonium ligands

Optimized geometry (minimized energy) of all organic ligands in free space was calculated using Gaussian 09W software, with a B3LYP/6-31G+(d,p) basis set. The results were visualized using GaussView 5.0 software, which also estimates the molecule's dipole moment.

SUPPLEMENTAL INFORMATION

Supplemental information can be found online at https://doi.org/10.1016/j.matt.2023.05.023.

ACKNOWLEDGMENTS

All authors acknowledge support from the National Science Foundation (NSF), award no. 2043205, and the Alfred P. Sloan Foundation, award no. FG-2022-18275. S.L.S. is partially supported by the UTK-ORNL science alliance program. The XRD and TEM characterizations were performed at the UTK-Institute for Advanced Materials & Manufacturing (IAMM) Diffraction Facility and Center for Microscopy.

AUTHOR CONTRIBUTIONS

Conceptualization, S.L.S., J.Y., and M.A.; methodology, J.Y. and M.A.; investigation, S.L.S., Y.T., J.Y., and M.A.; formal analysis, S.L.S.; data curation, S.L.S. and J.Y.; writing – original draft, S.L.S., J.Y., and M.A.; writing – review & editing, S.L.S., J.Y., and M.A.; visualization, S.L.S. and J.Y.; supervision, J.Y., B.H., and M.A.; resources, B.H. and M.A.; funding acquisition, M.A.

DECLARATION OF INTERESTS

The authors declare no competing interests.

Received: February 9, 2023
Revised: April 20, 2023
Accepted: May 9, 2023
Published: May 31, 2023

REFERENCES

1. Hoffman, J.B., Zaiats, G., Wappes, I., and Kamat, P.V. (2017). $CsPbBr_3$ solar cells: controlled film growth through layer-by-layer quantum dot deposition. Chem. Mater. *29*, 9767–9774. https://doi.org/10.1021/acs.chemmater.7b03751.

2. Li, C., Zang, Z., Chen, W., Hu, Z., Tang, X., Hu, W., Sun, K., Liu, X., and Chen, W. (2016). Highly pure green light emission of perovskite $CsPbBr_3$ quantum dots and their application for green light-emitting diodes. Opt Express *24*, 15071–15078. https://doi.org/10.1364/OE.24.015071.

3. Du, X., Wu, G., Cheng, J., Dang, H., Ma, K., Zhang, Y.-W., Tan, P.-F., and Chen, S. (2017). High-quality $CsPbBr_3$ perovskite nanocrystals for quantum dot light-emitting diodes. RSC Adv. *7*, 10391–10396. https://doi.org/10.1039/c6ra27665b.

4. Wei, C., Su, W., Li, J., Xu, B., Shan, Q., Wu, Y., Zhang, F., Luo, M., Xiang, H., Cui, Z., and Zeng, H. (2022). A universal ternary-solvent-ink strategy toward efficient inkjet-printed perovskite quantum dot light-emitting diodes. Adv. Mater. *34*, 2107798. https://doi.org/10.1002/adma.202107798.

5. Kim, Y.-H., Park, J., Kim, S., Kim, J.S., Xu, H., Jeong, S.-H., Hu, B., and Lee, T.-W. (2022). Exploiting the full advantages of colloidal perovskite nanocrystals for large-area efficient light-emitting diodes. Nat. Nanotechnol. *17*, 590–597. https://doi.org/10.1038/s41565-022-01113-4.

6. Shamsi, J., Urban, A.S., Imran, M., De Trizio, L., and Manna, L. (2019). Metal halide perovskite nanocrystals: synthesis, post-synthesis modifications, and their optical properties. Chem. Rev. *119*, 3296–3348. https://doi.org/10.1021/acs.chemrev.8b00644.

7. Nenon, D.P., Pressler, K., Kang, J., Koscher, B.A., Olshansky, J.H., Osowiecki, W.T., Koc, M.A., Wang, L.W., and Alivisatos, A.P. (2018). Design principles for trap-free $CsPbX_3$ nanocrystals: enumerating and eliminating surface halide vacancies with softer Lewis

bases. J. Am. Chem. Soc. *140*, 17760–17772. https://doi.org/10.1021/jacs.8b11035.

8. ten Brinck, S., Zaccaria, F., and Infante, I. (2019). Defects in lead halide perovskite nanocrystals: analogies and (many) differences with the bulk. ACS Energy Lett. *4*, 2739–2747. https://doi.org/10.1021/acsenergylett.9b01945.

9. Abir, S.S.H., Gupta, S.K., Ibrahim, A., Srivastava, B.B., and Lozano, K. (2021). Tunable $CsPb(Br/Cl)_3$ perovskite nanocrystals and further advancement in designing light emitting fiber membranes. Mater. Adv. *2*, 2700–2710. https://doi.org/10.1039/d1ma00183c.

10. Brown, A.A.M., Damodaran, B., Jiang, L., Tey, J.N., Pu, S.H., Mathews, N., and Mhaisalkar, S.G. (2020). Lead halide perovskite nanocrystals: room temperature syntheses toward commercial viability. Adv. Energy Mater. *10*, 2001349. https://doi.org/10.1002/aenm.202001349.

11. Sun, S., Yuan, D., Xu, Y., Wang, A., and Deng, Z. (2016). Ligand-mediated synthesis of shape-controlled cesium lead halide perovskite nanocrystals via reprecipitation process at room temperature. ACS Nano *10*, 3648–3657. https://doi.org/10.1021/acsnano.5b08193.

12. Huang, H., Raith, J., Kershaw, S.V., Kalytchuk, S., Tomanec, O., Jing, L., Susha, A.S., Zboril, R., and Rogach, A.L. (2017). Growth mechanism of strongly emitting CH3NH3PbBr3 perovskite nanocrystals with a tunable bandgap. Nat. Commun. *8*, 996. https://doi.org/10.1038/s41467-017-00929-2.

13. Jeong, W.H., Yu, Z., Gregori, L., Yang, J., Ha, S.R., Jang, J.W., Song, H., Park, J.H., Jung, E.D., Song, M.H., et al. (2021). In situ cadmium surface passivation of perovskite nanocrystals for blue LEDs. J. Mater. Chem. *9*, 26750–26757. https://doi.org/10.1039/D1TA08756H.

14. Song, H., Yang, J., Lim, S.G., Lee, J., Jeong, W.H., Choi, H., Lee, J.H., Kim, H.Y., Lee, B.R., and Choi, H. (2023). On the surface passivating principle of functional thiol towards efficient and stable perovskite nanocrystal solar cells. Chem. Eng. J. *454*, 140224. https://doi.org/10.1016/j.cej.2022.140224.

15. Chen, J., Jia, D., Zhuang, R., Hua, Y., and Zhang, X. (2022). Highly orientated perovskite quantum dot solids for efficient solar cells. Adv. Mater. *34*, 2204259. https://doi.org/10.1002/adma.202204259.

16. Jia, D., Chen, J., Qiu, J., Ma, H., Yu, M., Liu, J., and Zhang, X. (2022). Tailoring solvent-mediated ligand exchange for $CsPbI_3$ perovskite quantum dot solar cells with efficiency exceeding 16.5. Joule *6*, 1632–1653. https://doi.org/10.1016/j.joule.2022.05.007.

17. Kazes, M., Udayabhaskararao, T., Dey, S., and Oron, D. (2021). Effect of surface ligands in perovskite nanocrystals: extending in and reaching out. Acc. Chem. Res. *54*, 1409–1418. https://doi.org/10.1021/acs.accounts.0c00712.

18. Pan, A., He, B., Fan, X., Liu, Z., Urban, J.J., Alivisatos, A.P., He, L., and Liu, Y. (2016). Insight into the ligand-mediated synthesis of colloidal $CsPbBr_3$ perovskite nanocrystals: the role of organic acid, base, and cesium precursors. ACS Nano *10*, 7943–7954. https://doi.org/10.1021/acsnano.6b03863.

19. Yin, J., Yang, H., Gutiérrez-Arzaluz, L., Zhou, Y., Brédas, J.L., Bakr, O.M., and Mohammed, O.F. (2021). Luminescence and stability enhancement of inorganic perovskite nanocrystals via selective surface ligand binding. ACS Nano *15*, 17998–18005. https://doi.org/10.1021/acsnano.1c06480.

20. Quarta, D., Imran, M., Capodilupo, A.L., Petralanda, U., van Beek, B., De Angelis, F., Manna, L., Infante, I., De Trizio, L., and Giansante, C. (2019). Stable ligand coordination at the surface of colloidal $CsPbBr_3$ nanocrystals. J. Phys. Chem. Lett. *10*, 3715–3726. https://doi.org/10.1021/acs.jpclett.9b01634.

21. Shen, X., Kang, K., Yu, Z., Jeong, W.H., Choi, H., Park, S.H., Stranks, S.D., Snaith, H.J., Friend, R.H., and Lee, B.R. (2023). Passivation strategies for mitigating defect challenges in halide perovskite light-emitting diodes. Joule *7*, 272–308. https://doi.org/10.1016/j.joule.2023.01.008.

22. Hassan, Y., Park, J.H., Crawford, M.L., Sadhanala, A., Lee, J., Sadighian, J.C., Mosconi, E., Shivanna, R., Radicchi, E., Jeong, M., et al. (2021). Ligand-engineered bandgap stability in mixed-halide perovskite LEDs. Nature *591*, 72–77. https://doi.org/10.1038/s41586-021-03217-8.

23. Smock, S.R., Chen, Y., Rossini, A.J., and Brutchey, R.L. (2021). The surface chemistry and structure of colloidal lead halide perovskite nanocrystals. Acc. Chem. Res. *54*, 707–718. https://doi.org/10.1021/acs.accounts.0c00741.

24. Song, H., Yang, J., Jeong, W.H., Lee, J., Lee, T.H., Yoon, J.W., Lee, H., Ramadan, A.J., Oliver, R.D.J., Cho, S.C., et al. (2023). A universal perovskite nanocrystal ink for high-performance optoelectronic devices. Adv. Mater. *35*, 2209486. https://doi.org/10.1002/adma.202209486.

25. Imran, M., Ijaz, P., Baranov, D., Goldoni, L., Petralanda, U., Akkerman, Q., Abdelhady, A.L., Prato, M., Bianchini, P., Infante, I., and Manna, L. (2018). Shape-pure, nearly monodispersed $CsPbBr_3$ nanocubes prepared using secondary aliphatic amines. Nano Lett. *18*, 7822–7831. https://doi.org/10.1021/acs.nanolett.8b03598.

26. De Roo, J., Ibáñez, M., Geiregat, P., Nedelcu, G., Walravens, W., Maes, J., Martins, J.C., Van Driessche, I., Kovalenko, M.V., and Hens, Z. (2016). Highly dynamic ligand binding and light absorption coefficient of cesium lead bromide perovskite nanocrystals. ACS Nano *10*, 2071–2081. https://doi.org/10.1021/acsnano.5b06295.

27. Ravi, V.K., Santra, P.K., Joshi, N., Chugh, J., Singh, S.K., Rensmo, H., Ghosh, P., and Nag, A. (2017). Origin of the substitution mechanism for the binding of organic ligands on the surface of $CsPbBr_3$ perovskite nanocubes. J. Phys. Chem. Lett. *8*, 4988–4994. https://doi.org/10.1021/acs.jpclett.7b02192.

28. Heimbrook, A., Higgins, K., Kalinin, S.V., and Ahmadi, M. (2021). Exploring the physics of cesium lead halide perovskite quantum dots via Bayesian inference of the photoluminescence spectra in automated experiment. Nanophotonics *10*, 1977–1989. https://doi.org/10.1515/nanoph-2020-0662.

29. Akkerman, Q.A., Park, S., Radicchi, E., Nunzi, F., Mosconi, E., De Angelis, F., Brescia, R., Rastogi, P., Prato, M., and Manna, L. (2017). Nearly monodisperse insulator Cs_4PbX_6 (X = Cl, Br, I) nanocrystals, their mixed halide compositions, and their transformation into $CsPbX_3$ nanocrystals. Nano Lett. *17*, 1924–1930. https://doi.org/10.1021/acs.nanolett.6b05262.

30. Saidaminov, M.I., Almutlaq, J., Sarmah, S., Dursun, I., Zhumekenov, A.A., Begum, R., Pan, J., Cho, N., Mohammed, O.F., and Bakr, O.M. (2016). Pure Cs_4PbBr_6: highly luminescent zero-dimensional perovskite solids. ACS Energy Lett. *1*, 840–845. https://doi.org/10.1021/acsenergylett.6b00396.

31. Zou, S., Liu, C., Li, R., Jiang, F., Chen, X., Liu, Y., and Hong, M. (2019). From nonluminescent to blue-emitting Cs_4PbBr_6 nanocrystals: tailoring the insulator bandgap of 0D Perovskite through Sn cation doping. Adv. Mater. *31*, 1900606. https://doi.org/10.1002/adma.201900606.

32. Kondo, S., Amaya, K., and Saito, T. (2002). Localized optical absorption in Cs_4PbBr_6. J. Phys. Condens. Matter *14*, 2093–2099. https://doi.org/10.1088/0953-8984/14/8/334.

33. Li, Y., Huang, H., Xiong, Y., Kershaw, S.V., and Rogach, A.L. (2018). Reversible transformation between $CsPbBr_3$ and Cs_4PbBr_6 nanocrystals. CrystEngComm *20*, 4900–4904. https://doi.org/10.1039/C8CE00911B.

34. Wu, L., Hu, H., Xu, Y., Jiang, S., Chen, M., Zhong, Q., Yang, D., Liu, Q., Zhao, Y., Sun, B., et al. (2017). From nonluminescent Cs_4PbX_6 (X = Cl, Br, I) nanocrystals to highly luminescent $CsPbX_3$ nanocrystals: water-triggered transformation through a CsX-stripping mechanism. Nano Lett. *17*, 5799–5804. https://doi.org/10.1021/acs.nanolett.7b02896.

35. Palazon, F., Almeida, G., Akkerman, Q.A., De Trizio, L., Dang, Z., Prato, M., and Manna, L. (2017). Changing the dimensionality of cesium lead bromide nanocrystals by reversible postsynthesis transformations with amines. Chem. Mater. *29*, 4167–4171. https://doi.org/10.1021/acs.chemmater.7b00895.

36. Guan, M., Li, P., Wu, Y., Liu, X., Xu, S., and Zhang, J. (2022). Highly efficient green emission Cs_4PbBr_6 quantum dots with stable water endurance. Opt. Lett. *47*, 5020–5023. https://doi.org/10.1364/OL.471088.

37. Cha, J.H., Han, J.H., Yin, W., Park, C., Park, Y., Ahn, T.K., Cho, J.H., and Jung, D.Y. (2017). Photoresponse of $CsPbBr_3$ and Cs_4PbBr_6 perovskite single crystals. J. Phys. Chem. Lett. *8*, 565–570. https://doi.org/10.1021/acs.jpclett.6b02763.

38. Liu, Z., Bekenstein, Y., Ye, X., Nguyen, S.C., Swabeck, J., Zhang, D., Lee, S.T., Yang, P., Ma, W., and Alivisatos, A.P. (2017). Ligand mediated transformation of cesium lead bromide perovskite nanocrystals to lead depleted Cs_4PbBr_6 nanocrystals. J. Am. Chem. Soc. *139*, 5309–5312. https://doi.org/10.1021/jacs.7b01409.

39. Ma, Z., Li, F., Zhao, D., Xiao, G., and Zou, B. (2020). Whether or not emission of Cs_4PbBr_6 nanocrystals: high-pressure experimental evidence. CCS Chem. *2*, 71–80. https://doi.org/10.31635/ccschem.020.201900086.

40. Imran, M., Di Stasio, F., Dang, Z., Canale, C., Khan, A.H., Shamsi, J., Brescia, R., Prato, M., and Manna, L. (2016). Colloidal synthesis of strongly fluorescent $CsPbBr_3$ nanowires with width Tunable down to the quantum confinement regime. Chem. Mater. *28*, 6450–6454. https://doi.org/10.1021/acs.chemmater.6b03081.

41. Yuan, Y., Liu, Z., Liu, Z., Peng, L., Li, Y., and Tang, A. (2017). Photoluminescence and self-assembly of cesium lead halide perovskite nanocrystals: Effects of chain length of organic amines and reaction temperature. Appl. Surf. Sci. *405*, 280–288. https://doi.org/10.1016/j.apsusc.2017.02.024.

42. Almeida, G., Goldoni, L., Akkerman, Q., Dang, Z., Khan, A.H., Marras, S., Moreels, I., and Manna, L. (2018). Role of acid-base equilibria in the size, shape, and phase control of cesium lead bromide nanocrystals. ACS Nano *12*, 1704–1711. https://doi.org/10.1021/acsnano.7b08357.

43. Kerner, R.A., Schloemer, T.H., Schulz, P., Berry, J.J., Schwartz, J., Sellinger, A., and Rand, B.P. (2019). Amine additive reactions induced by the soft Lewis acidity of Pb^{2+} in halide perovskites. Part I: evidence for Pb–alkylamide formation. J. Mater. Chem. C *7*, 5251–5259. https://doi.org/10.1039/C8TC04871A.

44. Aharon, S., Wierzbowska, M., and Etgar, L. (2018). The effect of the alkylammonium ligand's length on organic–inorganic perovskite nanoparticles. ACS Energy Lett. *3*, 1387–1393. https://doi.org/10.1021/acsenergylett.8b00554.

45. Xie, C., He, J., Zhu, Y., Chen, L., and Yang, P. (2022). Roles of ligand and solvent for CsPbBr3 nanoplatelets. J. Lumin. *252*, 119400. https://doi.org/10.1016/j.jlumin.2022.119400.

46. Akkerman, Q.A., Motti, S.G., Srimath Kandada, A.R., Mosconi, E., D'Innocenzo, V., Bertoni, G., Marras, S., Kamino, B.A., Miranda, L., De Angelis, F., et al. (2016). Solution synthesis approach to colloidal cesium lead halide perovskite nanoplatelets with monolayer-level thickness control. J. Am. Chem. Soc. *138*, 1010–1016. https://doi.org/10.1021/jacs.5b12124.

47. Davis, A.H., Li, S., Lin, H., Chu, C., Franck, J.M., Leem, G., Maye, M.M., and Zheng, W. (2021). Ligand-mediated synthesis of chemically tailored two-dimensional all-inorganic perovskite nanoplatelets under ambient conditions. J. Mater. Chem. C *9*, 14226–14235. https://doi.org/10.1039/D1TC02931B.

48. Zhang, X., Zhou, Y., Peng, L., Lin, Z., Chang, Y., Zhou, Z., and Li, Y. (2022). Stable blue-emitting $CsPbBr_3$ nanoplatelets for lighting and display applications. ACS Appl. Nano Mater. *5*, 17012–17021. https://doi.org/10.1021/acsanm.2c03940.

49. Wu, Y., Lu, S., Ju, M.-G., Zhou, Q., and Wang, J. (2021). Accelerated design of promising mixed lead-free double halide organic–inorganic perovskites for photovoltaics using machine learning. Nanoscale *13*, 12250–12259. https://doi.org/10.1039/D1NR01117K.

50. Ahmad, M.U., Akib, A.R., Raihan, M.M.S., and Shams, A.B. (2022). ABO_3 perovskites' formability prediction and crystal structure classification using machine learning. Int. Con. Innov. Sci. Eng. Technol. *2022*, 480–485. https://doi.org/10.1109/ICISET54810.2022.9775906.

51. Zhao, Y., Zhang, J., Xu, Z., Sun, S., Langner, S., Hartono, N.T.P., Heumueller, T., Hou, Y., Elia, J., Li, N., et al. (2021). Discovery of temperature-induced stability reversal in perovskites using high-throughput robotic learning. Nat. Commun. *12*, 2191. https://doi.org/10.1038/s41467-021-22472-x.

52. Zhang, J., Li, Y., and Zhou, X. (2023). Machine-learning prediction of the comupted band gaps of double perovskite materials. Preprint at arXiv. https://doi.org/10.48550/arXiv.2301.03372.

53. Li, X., Dan, Y., Dong, R., Cao, Z., Niu, C., Song, Y., Li, S., and Hu, J. (2019). Computational screening of new perovskite materials using transfer learning and deep learning. Appl. Sci. *9*, 5510. https://doi.org/10.3390/app9245510.

54. Weerd, C.d., Lin, J., Gomez, L., Fujiwara, Y., Suenaga, K., and Gregorkiewicz, T. (2017). Hybridization of single nanocrystals of Cs_4PbBr_6 and $CsPbBr_3$. J. Phys. Chem. C *121*, 19490–19496. https://doi.org/10.1021/acs.jpcc.7b05752.

55. Koolyk, M., Amgar, D., Aharon, S., and Etgar, L. (2016). Kinetics of cesium lead halide perovskite nanoparticle growth; focusing and de-focusing of size distribution. Nanoscale *8*, 6403–6409. https://doi.org/10.1039/c5nr09127f.

56. Wang, L., Liu, H., Zhang, Y., and Mohammed, O.F. (2019). Photoluminescence origin of zero-dimensional Cs_4PbBr_6 perovskite. ACS Energy Lett. *5*, 87–99. https://doi.org/10.1021/acsenergylett.9b02275.

57. Li, M., Zhang, X., Dong, T., Wang, P., Matras-Postolek, K., and Yang, P. (2018). Evolution of morphology, phase composition, and photoluminescence of cesium lead bromine nanocrystals with temperature and precursors. J. Phys. Chem. C *122*, 28968–28976. https://doi.org/10.1021/acs.jpcc.8b10200.

58. Yang, J., Kim, M., Lee, S., Yoon, J.W., Shome, S., Bertens, K., Song, H., Lim, S.G., Oh, J.T., Bae, S.Y., et al. (2021). Solvent engineering of colloidal quantum dot inks for scalable fabrication of photovoltaics. ACS Appl. Mater. Interfaces *13*, 36992–37003. https://doi.org/10.1021/acsami.1c06352.

59. Hamill, J.C., Schwartz, J., and Loo, Y.-L. (2017). Influence of solvent coordination on hybrid organic–inorganic perovskite formation. ACS Energy Lett. *3*, 92–97. https://doi.org/10.1021/acsenergylett.7b01057.

60. Akkerman, Q.A., Nguyen, T.P.T., Boehme, S.C., Montanarella, F., Dirin, D.N., Wechsler, P., Beiglböck, F., Rainò, G., Erni, R., Katan, C., et al. (2022). Controlling the nucleation and growth kinetics of lead halide perovskite quantum dots. Science *377*, 1406–1412. https://doi.org/10.1126/science.abq3616.

61. Grisorio, R., Quarta, D., Fiore, A., Carbone, L., Suranna, G.P., and Giansante, C. (2019). The dynamic surface chemistry of colloidal metal chalcogenide quantum dots. Nanoscale Adv. *1*, 3639–3646. https://doi.org/10.1039/C9NA00452A.

62. Mardolcar, U.V., de Castro, C., and Santos, F.J.V. (1992). Dielectric constant measurements of toluene and benzene. Fluid Phase Equilib. *79*, 255–264. https://doi.org/10.1016/0378-3812(92)85135-U.

63. Tironi, I.G., and Van Gunsteren, W.F. (1994). A molecular dynamics simulation study of chloroform. Mol. Phys. *83*, 381–403. https://doi.org/10.1080/00268979400101331.

64. Qiu, J., Xue, W., Wang, W., and Li, Y. (2022). Effective surface passivation on $CsPbBr_3$ nanocrystals via post-treatment with aromatic carboxylic acid. Dyes Pigm. *198*, 109806. https://doi.org/10.1016/j.dyepig.2021.109806.

65. Zhang, X., Bai, X., Wu, H., Zhang, X., Sun, C., Zhang, Y., Zhang, W., Zheng, W., Yu, W.W., and Rogach, A.L. (2018). Water-assisted size and shape control of $CsPbBr_3$ perovskite nanocrystals. Angew. Chem. Int. Ed. *57*, 3337–3342. https://doi.org/10.1002/anie.201710869.

66. Liu, J., Song, K., Shin, Y., Liu, X., Chen, J., Yao, K.X., Pan, J., Yang, C., Yin, J., Xu, L.-J., et al. (2019). Light-induced self-assembly of cubic $CsPbBr_3$ perovskite nanocrystals into nanowires. Chem. Mater. *31*, 6642–6649. https://doi.org/10.1021/acs.chemmater.9b00680.

67. Bhardwaj, A., and Kushwaha, A.K. (2022). Capping ligands controlled structural and optoelectronic properties of $CsPbBr_3$ nanocrystals. J. Mater. Sci. Mater. Electron. *33*, 17404–17416. https://doi.org/10.1007/s10854-022-08622-x.

68. Sagle, L.B., Zhang, Y., Litosh, V.A., Chen, X., Cho, Y., and Cremer, P.S. (2009). Investigating the hydrogen-bonding model of urea denaturation. J. Am. Chem. Soc. *131*, 9304–9310. https://doi.org/10.1021/ja9016057.

69. Fiuza-Maneiro, N., Sun, K., López-Fernández, I., Gómez-Graña, S., Müller-Buschbaum, P., and Polavarapu, L. (2023). Ligand chemistry of inorganic lead halide perovskite nanocrystals. ACS Energy Lett. *8*, 1152–1191. https://doi.org/10.1021/acsenergylett.2c02363.

70. Smock, S.R., Williams, T.J., and Brutchey, R.L. (2018). Quantifying the thermodynamics of ligand binding to $CsPbBr_3$ quantum dots. Angew. Chem. Int. Ed. *57*, 11711–11715. https://doi.org/10.1002/anie.201806916.

71. Peng, C., Zhang, R., Chen, H., Liu, Y., Zhang, S., Fang, T., Guo, R., Zhang, J., Shan, Q., Jin, Y., et al. (2023). A demulsification–crystallization model for high-quality perovskite nanocrystals. Adv. Mater. *35*, 2206969. https://doi.org/10.1002/adma.202206969.